Natural Resources Canada | Ressources naturelles Canada

GEOMATICS CANADA
OPEN FILE 69

Recent ponding of upland ice-wedge polygon networks detected across the Canadian Arctic Archipelago using satellite remote sensing

R.H. Fraser, M. McFarlane-Winchester, and S.V. Kokelj

2023

Canada

GEOMATICS CANADA
OPEN FILE 69

Recent ponding of upland ice-wedge polygon networks detected across the Canadian Arctic Archipelago using satellite remote sensing

R.H. Fraser[1], M. McFarlane-Winchester[1], and S.V. Kokelj[2]

[1]Canada Centre for Mapping and Earth Observation, 580 Booth Street, Ottawa, Ontario
[2]Northwest Territories Geological Survey, Government of Northwest Territories, 4601-B 52 Avenue, Yellowknife, Northwest Territories

2023

Permanent link: https://doi.org/10.4095/329618

This publication is available for free download through GEOSCAN (https://geoscan.nrcan.gc.ca/).

Recommended citation
Fraser, R.H., McFarlane-Winchester, M., and Kokelj, S.V., 2023. Recent ponding of upland ice-wedge polygon networks detected across the Canadian Arctic Archipelago using satellite remote sensing; Geomatics Canada, Open File 69, 28 p. https://doi.org/10.4095/329618

Publications in this series have not been edited; they are released as submitted by the author.

Contents

1 Summary

Recent studies have demonstrated the sensitivity of cold, high-Arctic permafrost to rapid thaw. In Fraser et al. (2018), we showed that a series of anomalously warm summers in 1998 and 2010-2012 caused widespread, top-down thawing of hilltop ice-wedge networks across Banks Island (70 028 km^2) in the Canadian Arctic Archipelago. Several remote sensing datasets were used to identify numerous new ponds resulting from the melting of ice wedges and subsequent ground subsidence, or thermokarst. This Geomatics Canada Open File serves as a supplement to Fraser et al. (2018) by using similar, multi-scale remote sensing data to investigate the occurrence of upland ice-wedge thermokarst across a much larger 396 000 km^2 study domain in the Arctic Archipelago and Beaufort Coastlands. We show that ponded ice-wedge networks are common in semi-barren uplands and that, in 85% of visible ice-wedge polygon networks larger than 25 ha, a > 75% increase in ponding can be detected since the beginning of the 30 m Landsat satellite record in 1984. Large, upland ice-wedge melt ponds are frequently associated with ice-rich hummocky terrain, and they are generally less common and smaller in the warmer, ice-rich permafrost within the Yukon Coastal Plain and Tuktoyaktuk Coastlands. Similar to Banks Island, climate records from the expanded study domain suggest that warming temperatures are the primary driver of thermokarst. Records indicate an average annual 2.8 °C temperature increase over 52-74 years and that the 2010-2012 summers were 2.2 °C warmer than average.

2 Introduction

Ice wedges form when thermal contraction cracks in permafrost terrain fill with meltwater that freezes to form a vein of ice (Mackay 1974). Repeated cracking over hundreds or thousands of years can lead to the development of very large ice wedges up to several meters across (French 1974). Wedge ice is truncated by active layer thaw and in high Arctic uplands, shallow seasonal thaw and absence of disturbance results in wedge ice typically occurring 50-100 cm below the ground surface (Fraser et al. 2018; Farquharson et al. 2019). If the ground thermal regime changes due to either a disturbance (e.g. fire) that removes insulating organic material or due to a warming trend in summer temperatures, active layer thickness can increase and melt wedge ice (Jones et al. 2015; Farquharson et al. 2019). As ice volume is removed, the ground will subside along ice-wedge networks and the resulting thermokarst troughs can become ponded if they occur on relatively flat ground (Figure 1).

Figure 1. Ground and helicopter-based photos showing melt ponds in the uplands of eastern Banks Island resulting from recent ice-wedge thermokarst. Photos were taken by the Government of the Northwest Territories (Ecosystem Classification Group 2013) on July 23, 2011.

Ground-based and remote sensing observations have demonstrated that recent ice-wedge thermokarst is occurring in locations across the Arctic because of increased summer temperatures (Jorgenson et al. 2006; Liljedahl et al. 2016; Frost et al. 2018) and that this is also impacting colder, high-Arctic permafrost (Pollard et al. 2015; Fraser et al. 2018; Farquharson et al. 2019). Similarly, recent widespread thermokarst in the form of thaw slumping has been observed on high-Arctic hillslopes and attributed to recent warm summers (Segal et al. 2016; Rudy et al. 2017; Lewkowicz and Way 2019; Ward Jones 2019). These studies have shown that rapid thermokarst can occur in ice-rich,

formerly glaciated hummocky terrain where preserved massive ice lies close to the surface and receives little thermal buffering from the above mineral soils containing limited organic material (Kokelj et al. 2017; Fraser et al. 2018; Lewkowicz and Way 2019; Ward Jones 2019; Farquharson et al. 2019).

In Fraser et al. (2018) we documented recent and widespread thermokarst ponding of upland ice-wedge polygon networks (IWPN) across Banks Island (70 000 km^2) in the western Canadian Arctic Archipelago. This study used a combination of a 33-year Landsat image record, Sentinel-2 images, high-resolution historical air photos, high-resolution WorldView satellite imagery, and ground observations. We suggested that this type of ice-wedge thermokarst is likely impacting similar, upland ice-rich glaciated terrain in other Arctic tundra regions that have experienced warming.
In this Geomatics Canada Open File, we expand on this recent ice-wedge thermokarst analysis using similar remote sensing methods by documenting the occurrence of ice-wedge degradation in uplands across a 396 000 km^2 area within the Canadian Arctic Archipelago and Beaufort Sea coastal zone in Canada. We first map the broad distribution of upland IWPN within 15 km resolution grid cells and classify these as either showing ponding or no ponding using recent Sentinel-2 images. Large (> 25 ha) IWPN showing evidence of ponding are then delineated with Sentinel-2 and assessed using Landsat images to determine if the ponding has mostly occurred since ~ 1985. Finally, we corroborate these changes detected at 30 m using high-resolution, historical air photos from 1958-1974 and WorldView satellite images from 2012-2018 over nine, ~ 10 km^2 sites.

3 Methods

3.1 Study Region

The Arctic Archipelago portion of our 396 000 km^2 study region (Figure 2) lies in the Northern Arctic Terrestrial Ecozone (Ecosystem Classification Group 2013), which is characterized by continuous, cold permafrost (mean temperature at the top of permafrost (TTOP) <-6°C), low annual mean air temperatures (-11.6 to -19.2°C), and sparsely vegetated or barren uplands. The region was glaciated so tills and glaciofluvial deposits commonly characterize upland soils. The three mainland coastal zone portions of the study region along the Beaufort Sea lie in the Southern Arctic Ecozone, where milder temperatures support low shrub tundra vegetation in uplands just north of the treeline

(Ecosystem Classification Group 2012). Permafrost is continuous and mean TTOP in undisturbed terrain ranges from about -4 to -7 °C. The region hosts relict ice, wedge ice, and segregated ice (O'Neill et al., 2019).

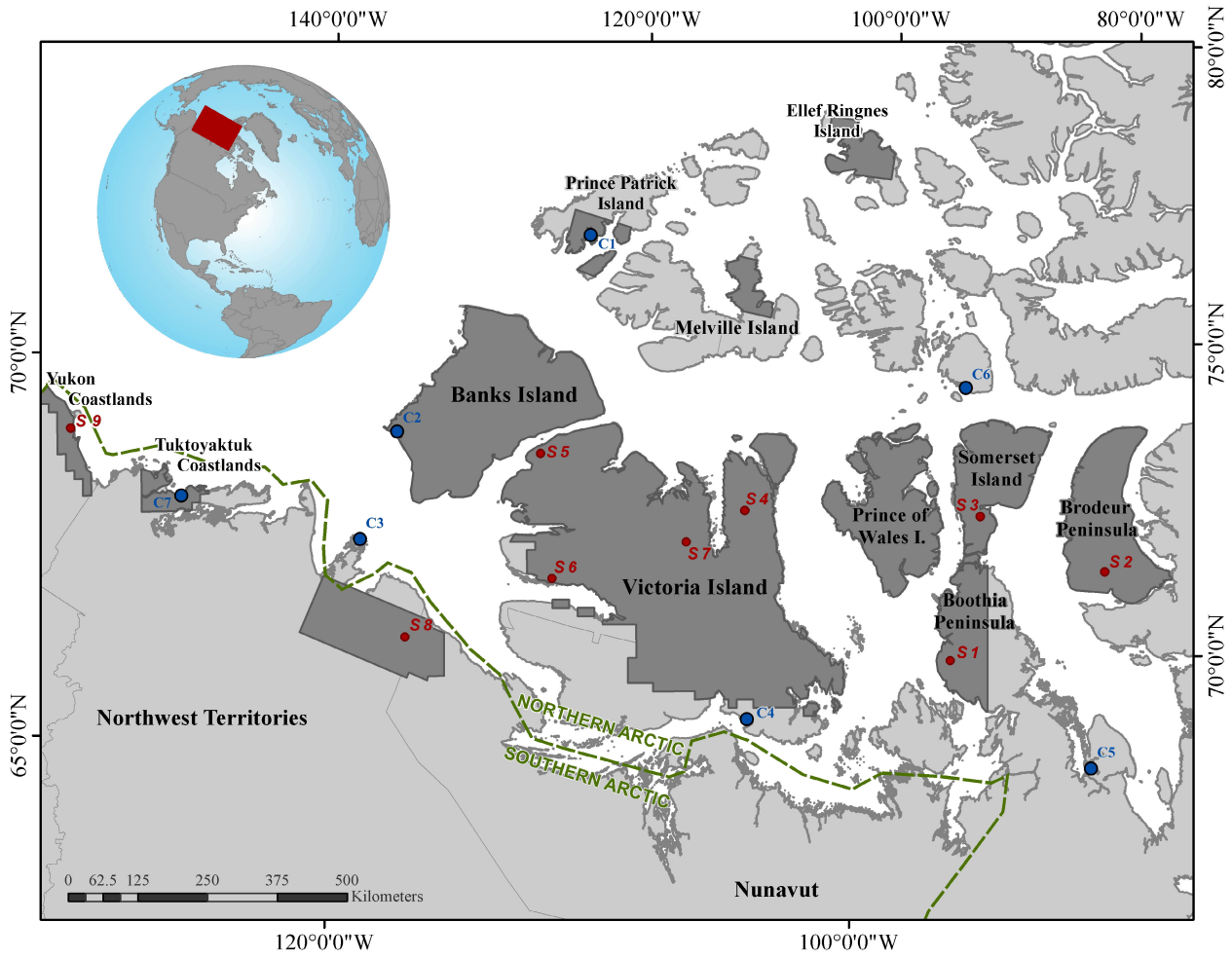

Figure 2. Study domain (dark grey shaded areas) for the satellite-based ice-wedge analysis covering 396 000 km^2 in Canada's Arctic. The "S" labels in red show the locations of nine, high resolution study sites, and the "C" labels show the locations of seven climate stations providing long-term temperature records (Table 5).

3.2 Mapping the broad distribution of upland ice-wedge terrain

The presence of well-developed, upland IWPN was mapped across the study domain by classifying 1 760, 15 km resolution grid cells (Kokelj et al. 2017) using manual interpretation of recent 10 m resolution Sentinel-2 satellite images (RGB = NIR, Red, Green). These grid cells were classified as (a) containing no evidence of polygonal terrain in sparsely vegetated uplands, (b) presenting evidence of upland ice-wedges from a polygonal pattern of troughs, but no visible melt ponds, or (c) presenting evidence of melt ponds along ice-wedge polygon troughs and at their intersections. In the two

westernmost coastal zone portions of the study region (Figure 2) where uplands typically support growth of continuous vegetation cover, we used the ArcticDEM from the Polar Geospatial Center to assist in delineating upland terrain. The use of Sentinel-2 images for this mapping provided consistent, recent coverage of the entire study domain, but will detect only well-developed IWPN and relatively severe thermokarst ponding visible at the 10 m pixel resolution. Our estimates of upland ice-wedge terrain occurrence and thermokarst ponding are accordingly conservative.

3.3 Delineating large uplands containing degraded ice-wedge networks and assessing their ponding changes

We digitized all upland IWPN areas larger than 25 ha (equivalent to 500 m by 500 m) that presented evidence of melt ponds in Sentinel-2 imagery from the previous step. The regions were delineated by the envelope formed by clusters of melt ponds located within 300 m of each other, such that results could be compared to the previous Banks Island study (Fraser et al. 2018). The 25 ha size threshold was chosen to require a reasonable degree of effort to delineate areas containing degraded IWPN over a very large study domain.

Melt pond changes occurring between 1985-1992 and 2012-2018 within each digitized IWPN were assessed using clear-sky, 30 m resolution Landsat short-wave infrared (SWIR) images. Ice-wedge melt ponds strongly absorb SWIR radiation and manifest as high spatial frequency texture in Landsat SWIR images (Fraser et al. 2018). By contrast, IWPN uplands with no melt ponds present a relatively uniform and high SWIR reflectance. The melt pond changes in each digitized upland IWPN area were classified according the following categories by overlaying and visually comparing the three sets of summer images (i.e. early Landsat SWIR, late Landsat SWIR, and recent 10 m Sentinel-2 RGB).

1. No IWPN melt ponds visible in the Sentinel-2 imagery are detectable in the 30 m Landsat SWIR imagery because they are smaller than the detection limit (Figure 3a).
2. None of the Sentinel-2 IWPN melt ponds detectable in the Landsat SWIR imagery show an increase in wetness (i.e. SWIR decrease) and evidence of ponding is similarly visible in both the early and late Landsat SWIR images.
3. Some, but fewer than 75% of the Sentinel-2 IWPN melt ponds detectable in the recent Landsat imagery are not detectable in the early Landsat SWIR imagery (i.e. the early

Landsat imagery appears uniform and not textured at these pond locations) (Figure 3b). This threshold represents a net change in ponding and thus accounts for less frequent cases where melt ponds are visible in the early Landsat imagery but have drained in the late Landsat imagery (these typically appears as circular patches of graminoid vegetation in the Sentinel-2 imagery).

4. More than 75% of the Sentinel melt pond locations detectable in the recent Landsat imagery are not detectable in the early Landsat SWIR imagery (Figure 3c). We used a 75% threshold since most degraded IWPN previously mapped on Banks Island would meet this criterion with an average 10-fold increase in ponding (Fraser et al. 2018).

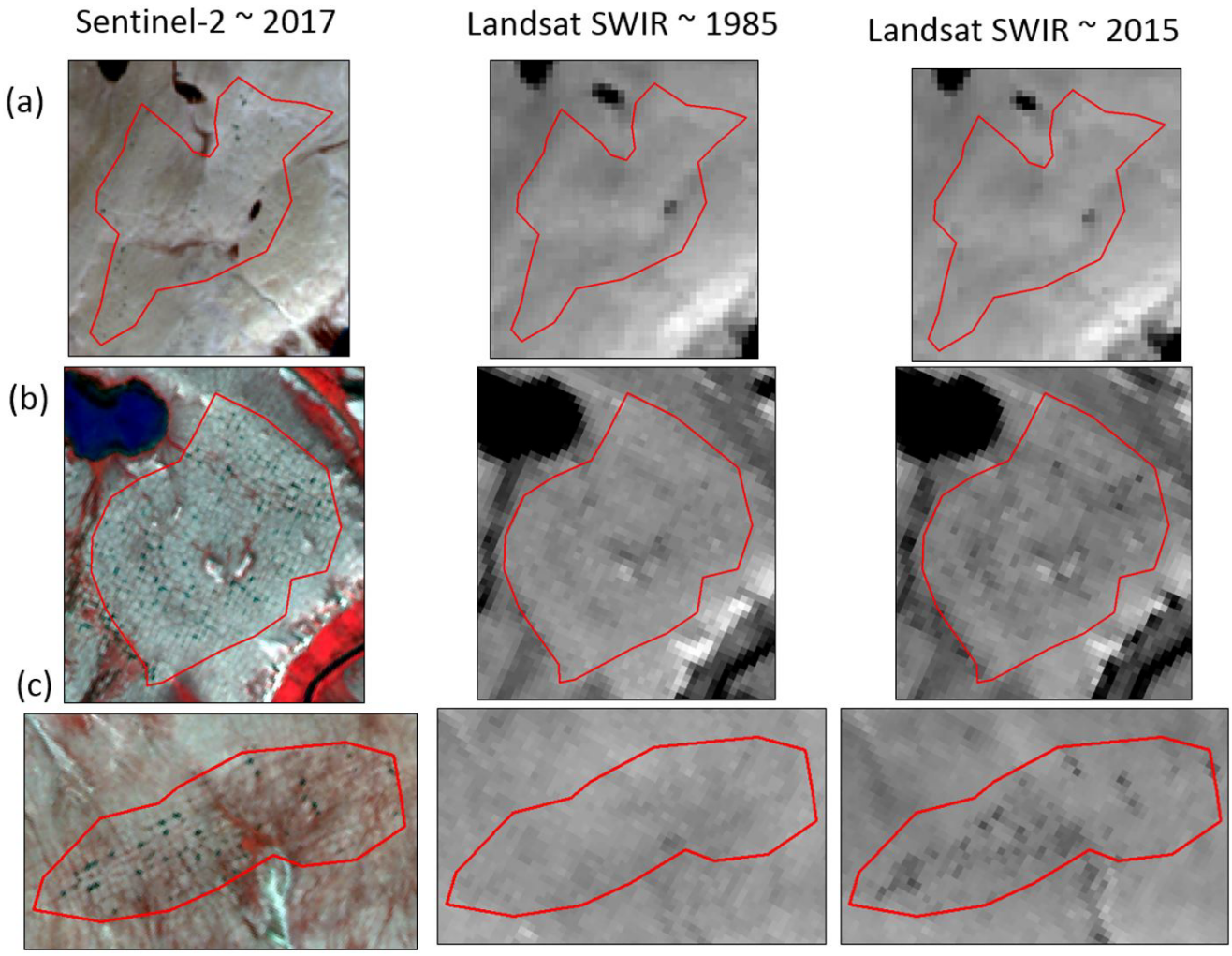

Figure 3. Example delineations of large (> 25 ha) IWPN showing evidence of thermokarst ponding in recent Sentinel-2 images and assessment of ponding changes using early (~ 1985) and late (~ 2015) Landsat SWIR images. Melt pond changes were classified as (a) smaller than the Landsat detection limit, no melt pond changes (not shown), (b) up to 75% of Sentinel-2 ponds detectable only in the recent Landsat imagery, and (c) more then 75% of ponds detectable only in the recent Landsat imagery.

We examined two, early-archive summer Landsat images (1985-1992) and conducted the comparison using the image exhibiting the greater degree of ponding, although in most cases the two early images were very similar in appearance. Therefore, all ponding change assessments were based on two early Landsat images and two late images (one being from Sentinel-2), which should partially account for any inter-annual variability in melt pond extents (Jorgenson et al. 2015). We opted not to derive long-term Landsat SWIR trends from a dense image stack for change detection as in Fraser et al. (2018), since this analysis suggested that a comparison of single-date SWIR changes provides an effective and sufficient indicator of long-term changes in ice-wedge ponding within upland terrain. A 30-year trend analysis was also made difficult by the relatively small number of early-archive Landsat 5 images providing clear and snow-free summer coverage for some northern portions of our study domain, with the exception of Banks Island.

3.4 Corroboration of ice-wedge degradation and ponding using high resolution images

We corroborated and more precisely characterized a selection of IWPN melt ponds delineated according to the above procedure using high-resolution summer images from nine, widely distributed sites ranging from 6.6-10.0 km^2 (Figure 1, Table 1). Historical, high-resolution imagery consisted of panchromatic NAPL air photos from 1958-1974 that can resolve melt ponds larger than about 1-4 m in extent depending on the photo scale (Table 1). Recent high-resolution images were from optical satellite sensors, providing 0.5 m resolution for summer dates between 2012 and 2018. We followed procedures in Fraser et al. (2018) to manually digitize melt ponds in the air photos and to extract them from the satellite images using image segmentation and thresholding. A minimum 16 m^2 pond size provided a consistent basis for comparing melt ponds for the two dates and to previous results for Banks Island (Fraser et al. 2018).

Table 1. Specifications for recent high-resolution satellite imagery and historical air photos from the Canadian National Air Photo Library (NAPL) covering the high resolution study areas. Mid to late summer dates were selected to avoid the period of snowmelt and high spring runoff.

Study Site ID	Location (lat, lon)	Area (km^2)	Satellite	Resolution (m)	Date	Historical Air Photo Date	Air Photo Scale
1	70.28, -95.89	6.6	WorldView-1	0.5 (Pan)	August 28, 2012	July 30, 1958	1:60 000
2	71.55, -88.10	7.9	WorldView-2	0.5 (Pan)	August 20, 2013	July 22, 1958	1:60 000
3	72.60, -94.33	9.0	WorldView-2	0.5 (Pan) 2.0 (MS)	August 19, 2012	July 14, 1973	1:25 000
4	72.44, -106.71	9.6	WorldView-1	0.5 (Pan)	July 16, 2015	August 11, 1958	1:60 000
5	72.54, -117.92	10.0	Quickbird-2	0.6 (Pan) 2.4 MS	August 2, 2012	August 28, 1959	1:60 000
6	70.66, -115.49	7.1	WorldView-2	0.5 (Pan) 2.0 (MS)	July 19, 2014	August 10, 1961	1:100 000
7	71.76, -109.38	8.6	Quickbird-2	0.5 (Pan)	August 13, 2013	July 15, 1958	1:60 000
8	69.01, -121.06	8.9	GeoEye-1	0.5 (Pan) 1.8 (MS)	August 12, 2014	July 23, 1974	1:60 000
9	69.35, -138.93	7.1	WorldView-2	0.5 (Pan) 2.0 (MS)	July 23, 2018	August 28, 1970	1:25 000

4 Results

Figure 4 shows the distribution of upland IWPN across the study domain, identified using Sentinel-2 imagery. Within this 396 000 km^2 area, no upland IWPN were detected within 15 km grid cells that covered 142 200 km^2 (36% of the area). IWPN with no ponding were detected within grid cells that covered 27 225 km^2 (7%) and IWPN with visible ponding were detected over 226 575 km^2 (57%).

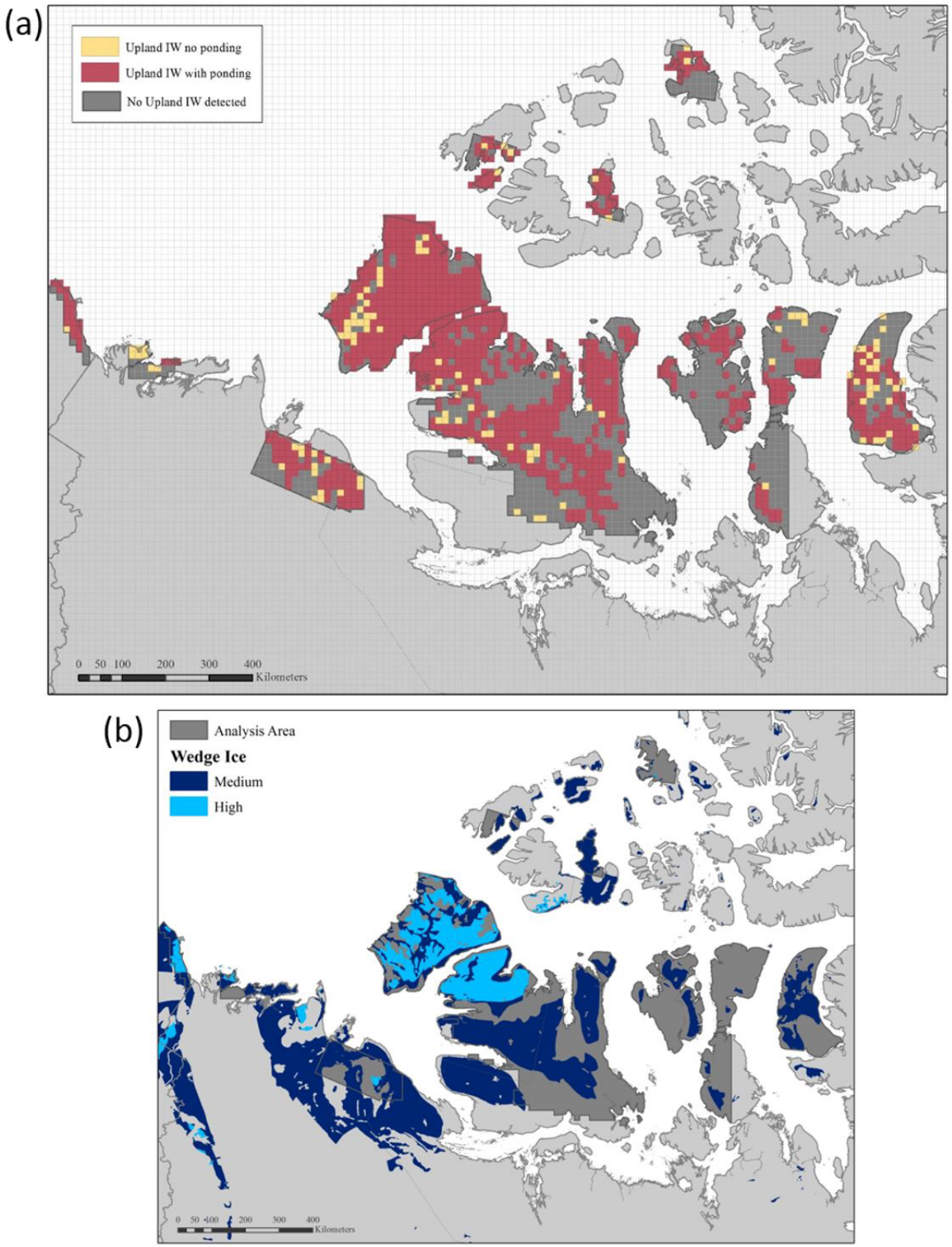

Figure 4. (a) Distribution of upland IWPN across the study domain identified using Sentinel-2 imagery, and (b) the distribution of medium and high wedge ice abundance in Canada modeled by O'Neill et al. (2019).

Table 2 summarizes the Landsat-based change severity classes assigned to 1 214 ponded upland IWPN > 25 ha delineated as polygons using the Sentinel-2 imagery. Together, these cover 1 527 km^2 (0.7%) of the 226 575 km^2 area of 15 km grid cells where upland ponding was observed in the Sentinel-2 imagery. We found that the majority of digitized IWPN (77%) and total IWPN area (85%) showed more than a 75% increase in upland ponding detected using multi-temporal Landsat SWIR images. Figure 5 displays at 15 km resolution, the percent coverage of large (> 25 ha) IWPN demonstrating evidence of increased ponding (classes 3-4 in Table 2). The most severely impacted regions occur on Banks Island (results from Fraser et al. 2018), northwest Victoria Island, and central Victoria Island. The four higher-Arctic Islands and mainland sites had little or no increase in ponding that could be detected using multitemporal Landsat SWIR images. None of the IWPN delineated across the study domain showed evidence of a net decrease in ponding since ~ 1985.

Table 2. Number and area of large (> 25 ha) upland IWPN areas that were digitized using Sentinel-2 imagery. Each digitized area was assigned a severity class based on interpretation of Landsat SWIR images.

IWPN Change Severity Class	**Number of IWPN (%)**	**IWPN Area in km^2 (%)**
1. Ponds below Landsat detection limit	116 (9.6)	80 (5.2)
2. No net change in ponding	16 (1.3)	14 (0.9)
3. < 75% increase in ponding	144 (11.9)	131 (8.5)
4. > 75% increase in ponding	938 (77.3)	1 312 (85.4)
Total	1 214	1 537

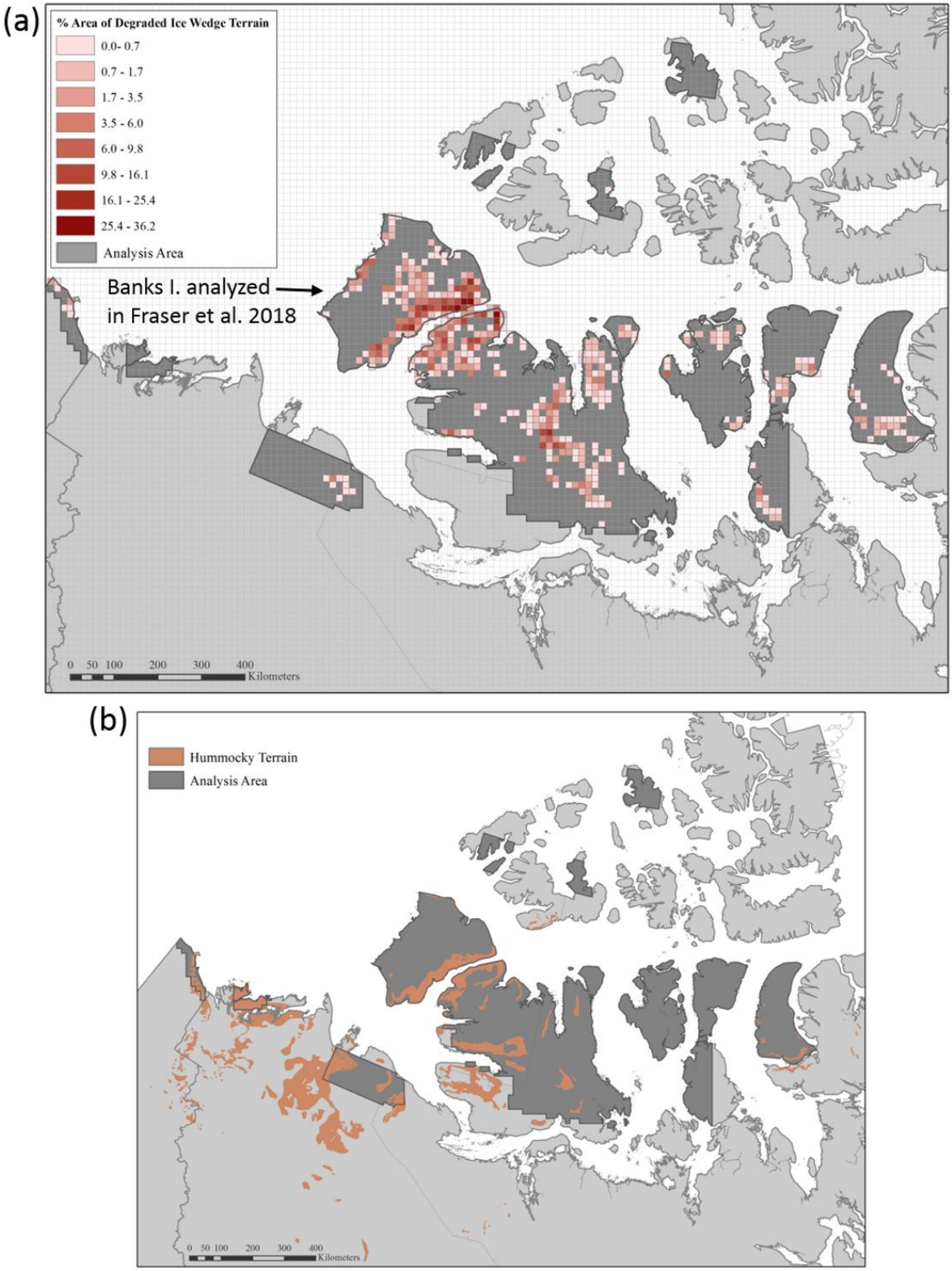

Figure 5. (a) Percent coverage of large (> 25 ha) IWPN demonstrating evidence of increased ponding since 1985, summarized within 15 km resolution cells, and (b) the distribution of ice-rich hummocky moraine mapped by Prest et al. (1968).

The change analyses conducted at higher resolution for the nine, widely distributed study sites showed consistent increases in pond density and area between 1958-1974 and 2012-2018 (Table 3). Average upland ice-wedge pond area increased nearly tenfold, from 0.06% to 0.53%. Figure 6 shows (a) the historical air photo and (b) the recent WorldView image over a portion of site 2 on the Brodeur Peninsula. The Sentinel-2 image (c) and Landsat images (d-e) used to delineate the ponded IWPN are also presented. In the 1958 air photo, IWPN troughs can be discerned in some areas, but the number of ponds is very small in relation to the 2013 WorldView image, where several ponds > 100 m^2 are shown in the enlargement. Corresponding high-resolution images for the other eight study sites are shown in Figure A1.

Table 3. Comparison of ice-wedge melt pond characteristics between the two mapping periods for nine upland study sites. The table also includes the averages of the nine study sites and of the eight previous study sites on Banks Island (Fraser et al. 2018).

		1958-1974 Air Photos			**2012-2018 High Resolution Satellite Imagery**				**Percent Change**	
Study Area ID	Area (km^2)	Avg. pond area (m^2)	Pond area (ha) per km^2 (or %)	Density (ponds /km^2)	Avg. pond area (m^2)	Pond area (ha) per km^2 (or %)	Density (ponds /km^2)	Largest New Pond (m^2)	Total pond area	Pond density
1	6.6	106	0.08	7.2	88	0.99	111.6	885	1 179%	1 444%
2	7.9	72	0.01	0.9	66	0.16	24.3	308	2 379%	2 629%
3	9	43	0.00	0.3	64	0.82	128.8	615	56 874%	38 400%
4	9.6	40	0.01	3.0	85	0.67	78.5	819	5 356%	2 486%
5	10	157	0.00	0.3	91	0.11	12.1	419	2 255%	3 967%
6	7.1	263	0.20	7.7	118	0.79	66.5	700	287%	760%
7	8.6	146	0.05	3.4	103	0.12	11.7	347	143%	245%
8	8.9	107	0.14	13.5	97	0.59	60.8	522	311%	352%
9	7.1	47	0.01	2.3	60	0.21	35.1	774	1 889%	1 456%
Average	**8.5**	**47**	**0.06**	**4.5**	**89**	**0.53**	**61.8**	**577**	**645%**	**1 259%**
Average Banks I.	**8.9**	**133**	**0.2**	**13.4**	**117**	**1.5**	**118.6**	**1 057**	**923%**	**784%**

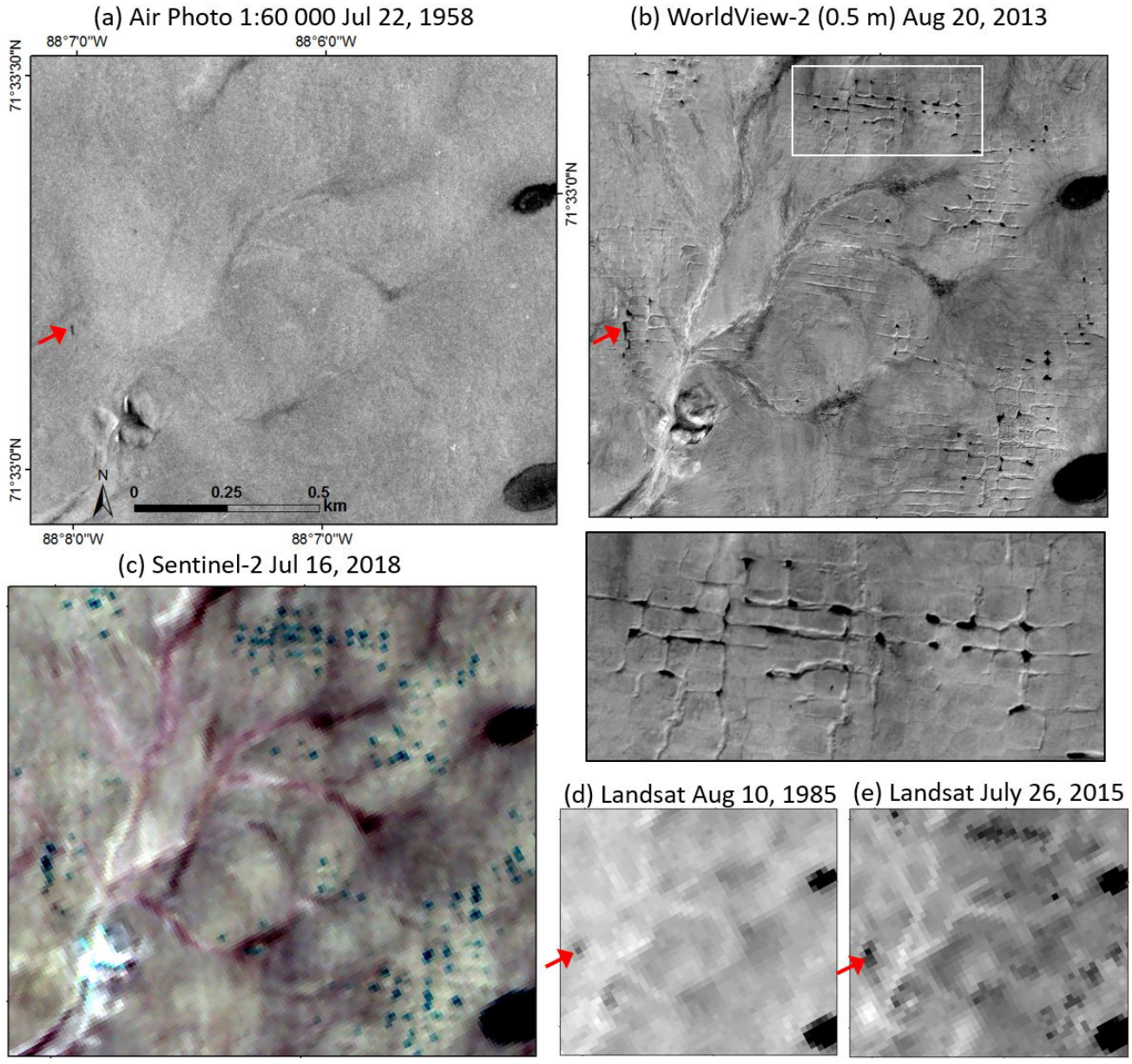

Figure 6. Portion of high resolution study site 2 on the Brodeur Peninsula (Fig. 1) showing (a) the historical air photo, (b) recent WorldView image, and the (c) Sentinel-2 image and (d-e) Landsat images that were used to delineate the ponded IWPN. Melt pond area changes for the nine high resolution study sites are summarized in Table 3.

5 Discussion

Our results demonstrate the widespread distribution of upland IWPN across Canada's Central and Western, mid-to-high Arctic (Figure 4a) and are consistent with the modelled abundance of wedge ice in continuous permafrost (Figure 4b; O'Neill et al. 2019). Landsat-based change detection also demonstrates that recent thermokarst ponding of upland ice wedges is a broad-scale phenomenon (Figure 5a), especially within ice-rich hummocky terrain containing massive ice (Figure 5b; Prest et al.

1968). The percent composition of surficial geology types (O'Neill et al. 2019) for ice-wedge terrain (Figure 4a) and the digitized, recently ponded IWPN (aggregated in Figure 5a) is shown in Figure 7. Both contain a greater proportion of the hummocky terrain and till hummocky types than would be expected based on surficial geology composition within the 396 000 km^2 study domain (blue bars).

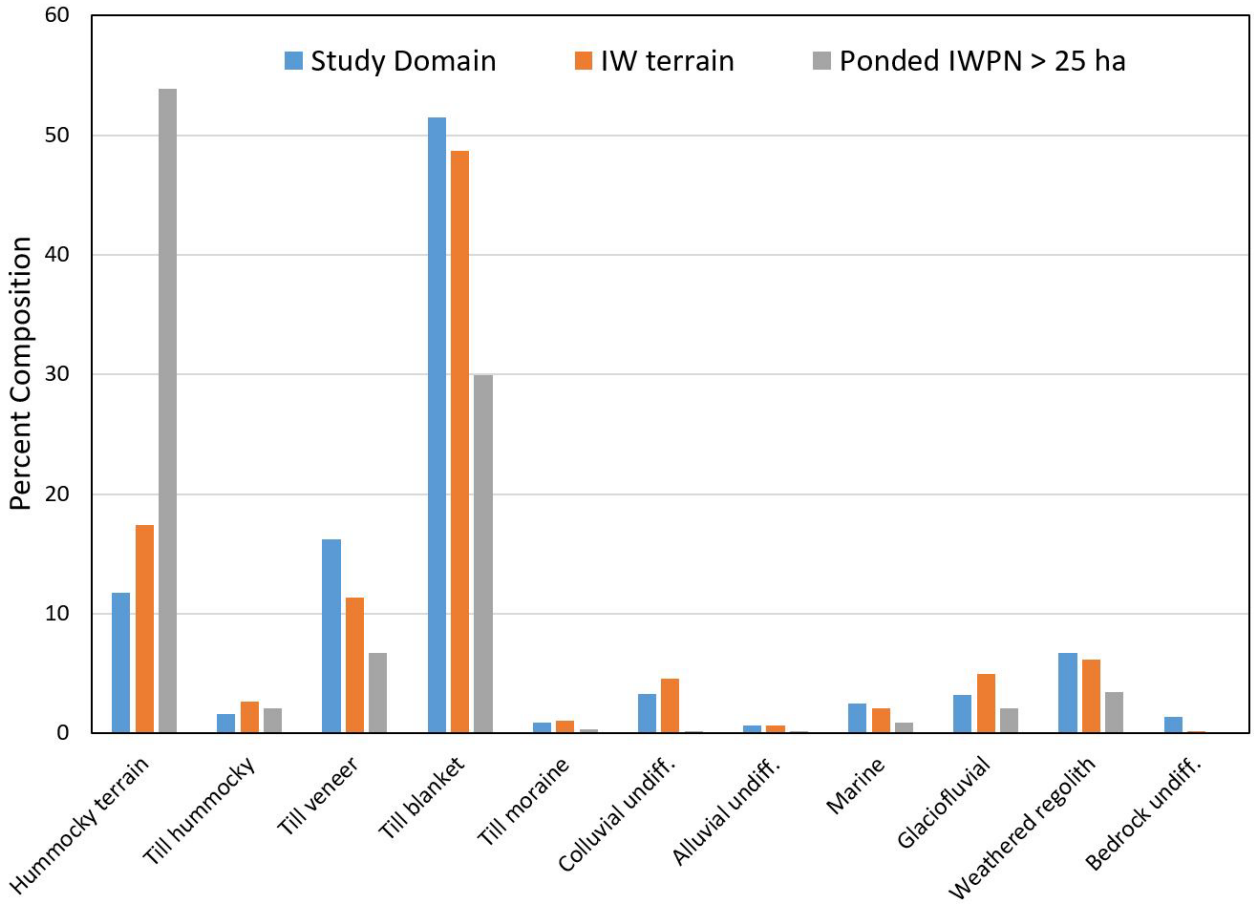

Figure 7. The percent composition of surficial geology types within (a) the entire 396 000 km^2 study domain (blue bars), (b) the 220 297 km^2 of the study domain in which the 15 km cells contain upland ice-wedge terrain (orange bars), and (c) the 1 527 km^2 of digitized, recently ponded IWNP > 25 ha (grey bars). Surficial geology was simplified from O'Neill et al. (2019).

The four most northerly Arctic islands examined showed evidence of sparser and smaller upland IWPN (Figure 4a), but contained only 11 IWPN areas meeting the size threshold (25 ha) to be included in the Landsat pond change analysis. Only one of these areas on Melville Island showed evidence that large melt ponds had developed within the past few decades (Figure 4a).

The greatest concentration of large IWPN showing recent ponding is located in the lower Arctic Archipelago portion of the study region (Figure 5a). Here, thermokarst sensitivity is high because

large, previously undisturbed ice wedges typically lie close to the ground surface under mineral soils that provide little thermal buffering from warm summer temperatures (Fraser et al. 2018; Farquharson et al. 2019). By contrast, the warmest and most densely vegetated region studied was the Tuktoyaktuk Coastlands (Figure 2), which showed limited evidence of upland IWPN (Figure 4a) and no evidence of IWPN > 25 ha impacted by recent thermokarst ponding (Figure 5a). Although upland IWPN are common in this region (Kokelj et al. 2014), they are more difficult to detect both in satellite imagery and on the ground since their trough extents, widths, and depths are smaller, and are obscured by a near-continuous cover of vegetation (Morse and Burn 2013; Kokelj et al. 2014). We also observed limited evidence of upland IWPN or ponding in this ice-rich region when examining ~ 0.5 m resolution optical satellite imagery and low-level aerial photographs (Figure 8).

Figure 8. Pan-sharpened (0.6 m) Quickbird satellite image (July 26, 2012) and GNWT low-level oblique air photo (July 16, 2009) along the Tuktoyaktuk Highway 9 km south of Tuktoyaktuk, NWT. Upland IWPN are difficult to discern in this region because they are obscured by a near-continuous cover of shrub vegetation, while upland thermokarst melt ponds are relatively rare.

The Yukon Coastlands (Figure 2) had more ponded IWPN compared to the Tuktoyaktuk Coastlands (Figure 4a), but only a limited number of large (> 25 ha) upland areas demonstrated recent ponding in the Landsat SWIR imagery (Figure 5a). By contrast, the high-resolution images examined in this region clearly show increases in ponding since 1970 (site #9 Figure A1). The major reason for this scale-dependent difference is that melt ponds in this region are generally smaller (averaging 60 m^2) than those in the higher-Arctic study regions (Table 3), and few are larger than the Landsat detection limit (site # 9 Figure A1d-e). To better characterize this limit, we examined the sizes of 60 upland melt ponds that were detectable in Landsat SWIR images within four areas of high-resolution satellite coverage. The smallest detectable pond was 130 m^2 and the median was 198 m^2, or 22% of a Landsat pixel area.

Regional climate data suggest that the recent, widespread ice-wedge degradation had been caused by warming temperatures (Fraser et al. 2018). Homogenized temperature records (Mekis and Vincent 2011) from seven weather stations bounding the study domain (Figure 2) were used to compute trends based on monthly mean air temperature (Table 4). The region shows consistent positive trends in both annual temperature (avg. +2.8 °C) and June-August summer temperature (avg. +1.5 °C) over the past 52-74 years. An Arctic cooling trend during at least the past 2 000 years following the Holocene Thermal Maximum was reversed during the last century (Kaufman et al. 2009; Briner et al. 2016), and recent summer temperatures in some Canadian Arctic regions may be unprecedented for more than 13 000 years (Porter et al. 2019), and as much as 115 000 years (Pendleton et al. 2019).

The summers of 2010-2012 were particularly warm within our study region, with temperatures averaging 2.2 °C higher than the long-term summer mean and 2.8 °C higher than summer temperatures at the beginning of climate records, predicted using the regression trends (Table 4). During this 2010-2012 period, rapid thermokarst was observed as increased ice-wedge subsidence and ponding on Banks Island (Fraser et al. 2018; Farquharson et al. 2019), and as proliferating thaw slumps over Banks Island (Lewkowicz and Way 2019) and the high-Arctic Eureka Sound Lowlands (Ward Jones et al. 2019).

Table 4. Summary of homogenized temperature data from seven climate stations bounding the study domain (Figure 1).

Station	Period of Record	Rate of Annual Change (°C/yr)	Total Annual Change (°C)	Rate of Summer Change (°C/yr)	Total Summer Change (°C)	Summers 2010-12 vs Average	Summers 2010-12 vs Earliest Date Pred.
1. Mould Bay	1948-2016	0.038**	2.5	0.020*	1.3	2.0	2.7
2. Sachs Harbour	1956-2016	0.058**	3.4	0.029*	1.7	3.1	4.0
3. Cape Parry	1957-2017	0.044**	2.4	0.022*	1.3	1.8	2.5
4. Cambridge Bay	1940-2014	0.035**	2.6	0.018*	1.4	1.5	2.2
5. Pelly Bay	1959-2011	0.065**	3.2	0.048**	2.5	1.8	3.0
6. Resolute Bay	1948-2016	0.036**	2.4	0.012 (p=0.11)	0.8	2.5	2.9
7. Tuktoyaktuk	1958-2016	0.050**	2.9	0.031**	1.8	1.8	2.7
Average		**0.047**	**2.8**	**0.026**	**1.5**	**2.2**	**2.8**

*p<0.05
**p<0.01

6 Summary

- We extended a remote sensing analysis of ice-wedge thermokarst and ponding on Banks Island (70 028 km^2) (Fraser et al. 2018) to a region in the Canadian Arctic Archipelago and Beaufort Sea Coastlands covering 396 000 km^2.
- IWPN with visible ponding were detected within 15 km grid cells covering 226 575 km^2 (57% of the study region).
- We delineated 1 214 upland IWPN larger than 25 ha using Sentinel-2 imagery and found that 77% demonstrate a > 75% increase in ponding based on interpretation of Landsat SWIR images from 1985-1992 and 2012-2018.
- Recently ponded IWPN are closely associated with ice-rich, hummocky surficial geology types.
- Ice-wedge melt pond change analyses conducted at higher resolution for nine, ~ 10 km^2 study sites showed consistent increases in pond density (1 259%) and area (645%) between 1958-1974 and 2012-2018 and thus corroborate changes observed using coarser resolution satellite imagery.

- The recent, widespread upland ice-wedge degradation and ponding was likely caused by climate warming, in which regional average annual temperature increased by 2.8 °C and summer temperature increased by 1.5 °C during the past 52-74 years.

7 Acknowledgements

Funding was provided by the Canadian Space Agency Government Related Initiatives Program under the project "Big Data Analytics of Earth Observation Data in Support of Evidence-Based Decision Making for Climate Change." The ArcticDEM products were provided by the Polar Geospatial Center under NSF OPP awards 1043681, 1559691 and 1542736. We thank Yu Zhang for his helpful review of this report.

8 References

Briner, J. P. et al. 2016. Holocene climate change in Arctic Canada and Greenland. Quaternary Science Reviews, 147: 340–364.

Ecosystem Classification Group. 2012. Ecological regions of the Northwest Territories—Southern Arctic. Department of Environment and Natural Resources, Government of the Northwest Territories, Yellowknife, NT, Canada. 170 pp. + insert map

Ecosystem Classification Group. 2013. Ecological regions of the Northwest Territories—Northern Arctic. Department of Environment and Natural Resources, Government of the Northwest Territories, Yellowknife, NT, Canada. 157 pp. + insert map

French, H.M. 1974. Active Thermokarst Processes, Eastern Banks Island, Western Canadian Arctic. Canadian Journal of Earth Sciences, 11: 785–794.

Farquharson, L.M., Romanovsky, V.E., Cable, W.L., Walker, D.A., Kokelj, S.V., and Nicolsky, D. 2019. Climate change drives widespread and rapid thermokarst development in very cold permafrost in the Canadian High Arctic. Geophysical Research Letters, 46.

Fraser, R.H., Kokelj, S.V., Lantz, T.C., McFarlane-Winchester, M., Olthof, I., and Lacelle, D. 2018. Climate sensitivity of high Arctic permafrost terrain demonstrated by widespread ice-wedge thermokarst on Banks Island. Remote Sensing, 10: 954.

Frost, G.V., Christopherson, T., Jorgenson, M.T., Liljedahl, A.K., Macander, M.J., Walker, D.A., and Wells, A.F. 2018. Regional patterns and asynchronous onset of ice-wedge degradation since the mid-20th century in Arctic Alaska. Remote Sensing, 10: 1312.

Jones, B.M., Grosse, G., Arp, C.D., Miller, E., Liu, L., Hayes, D.J., and Larsen, C.F. 2015. Recent Arctic tundra fire initiates widespread thermokarst development. Scientific Reports, 5: 15865.

Jorgenson, M.T., Shur, Y.L., and Pullman, E.R. 2006. Abrupt increase in permafrost degradation in Arctic Alaska. Geophysical Research Letters, 33: L02503.

Jorgenson, M.T., Kanevskiy, M., Shur, Y., Moskalenko, N., Brown, D.R.N., Wickland, K., Striegl, R., and Koch, J. 2015. Role of ground ice dynamics and ecological feedbacks in recent ice wedge degradation and stabilization. Journal of Geophysical Research: Earth Surface, 120: 2280–2297.

Kaufman, D.S., Schneider, D.P., McKay, N.P., Ammann, C.M., Bradley, R.S., Briffa, K.R., Miller, G.H., Otto-Bliesner, B.L., Overpeck, J.T., Vinther, B.M., and Arctic Lakes 2k Project Members. 2009. Recent Warming Reverses Long-Term Arctic Cooling. Science, 325: 1236–1239.

Kokelj, S.V., Lantz, T.C., Wolfe, S.A., Kanigan, J.C., Morse, P.D., Coutts, R., Molina-Giraldo, N., and Burn, C.R. 2014. Distribution and activity of ice wedges across the forest-tundra transition, western Arctic Canada. Journal of Geophysical Research: Earth Surface, 119: 2032–2047.

Kokelj, S.V., Lantz, T.C., Tunnicliffe, J., Segal, R., and Lacelle, D. 2017. Climate-driven thaw of permafrost preserved glacial landscapes, northwestern Canada. Geology, 45: 371–374.

Lewkowicz, A.G., and Way, R.G. 2019. Extremes of summer climate trigger thousands of thermokarst landslides in a High Arctic environment. Nature Communications, 10: 1329.

Liljedahl, A.K., Boike, J., Daanen, R.P., Fedorov, A.,N., Frost, G.V., Grosse, G., Hinzman, L.D., Iijma, Y., Jorgenson, J.C., Matveyeva, N., Necsoiu, M., Raynolds, M.K., Romanovsky, V.E., Schulla, J., Tape, K.D., Walker, D.A., Wilson, C. J., Yabuki, H., and Zona, D. 2016. Pan-Arctic ice-wedge degradation in warming permafrost and its influence on tundra hydrology. Nature Geoscience, 9: 312.

Mackay, J.R. 1974. Ice-wedge cracks, Garry Island, Northwest Territories. Canadian Journal of Earth Sciences, 11: 1366–1383.

Mekis, É., and Vincent, L.A. 2011. An overview of the second generation adjusted daily precipitation dataset for trend analysis in Canada. Atmosphere-Ocean, 49: 163–177.

Morse, P.D., and C.R. Burn. 2013. Field observations of syngenetic ice wedge polygons, outer Mackenzie Delta, western Arctic coast, Canada, Journal of Geophysical Research: Earth Surface, 118: 1320–1332.

O'Neill, H.B., Wolfe, S.A., and Duchesne, C. 2019. New ground ice maps for Canada using a paleogeographic modelling approach. The Cryosphere, 13: 753–773.

Pendleton, S.L., Miller, G.H., Lifton, N., et al. 2019. Rapidly receding Arctic Canada glaciers revealing landscapes continuously ice-covered for more than 40,000 years. Nature Communications, 10: 445.

Pollard, W.H., Ward, M.K., and Becker, M.S. 2015. The Eureka Sound Lowlands: an ice-rich permafrost landscape in transition. GeoQuebec 2015 – the 68th Canadian Geotechnical Conference and the 7th

Canadian Permafrost Conference Proceedings, 2015, http://members.cgs.ca/documents/conference2015/GeoQuebec/papers/402.pdf

Porter, T.J., Schoenemann, S.W., Davies, L.J. et al. 2019. Recent summer warming in northwestern Canada exceeds the Holocene thermal maximum. Nature Communications, 10: 1631.

Prest, V.K., Grant, D.R., and Rampton, V.N. 1968. Glacial map of Canada. Geological Survey of Canada, Map 1253A.

Rudy, A.C.A., Lamoureux, S.F., Kokelj, S.V., Smith, I.R., and England, J.H. 2017. Accelerating thermokarst transforms ice-cored terrain triggering a downstream cascade to the ocean. Geophysical Research Letters, 44: 2017GL074912.

Segal, R.A., Lantz, T.C., and Kokelj, S.V. 2016. Acceleration of thaw slump activity in glaciated landscapes of the Western Canadian Arctic. Environmental Research Letters, 11: 034025.

Ward Jones, M.K., Pollard, W.H., and Jones, B.M. 2019. Rapid initialization of retrogressive thaw slumps in the Canadian high Arctic and their response to climate and terrain factors. Environmental Research Letters, 14: 055006.

Appendix Figure 1. Portions of high resolution study sites 1 and 3-9 (Fig. 1) showing (a) the historical air photo, (b) recent WorldView image, and the (c) Sentinel-2 image and (d-e) Landsat images that were used to delineate the ponded IWPN. Melt pond area changes for the nine high-resolution study sites are summarized in Table 3.

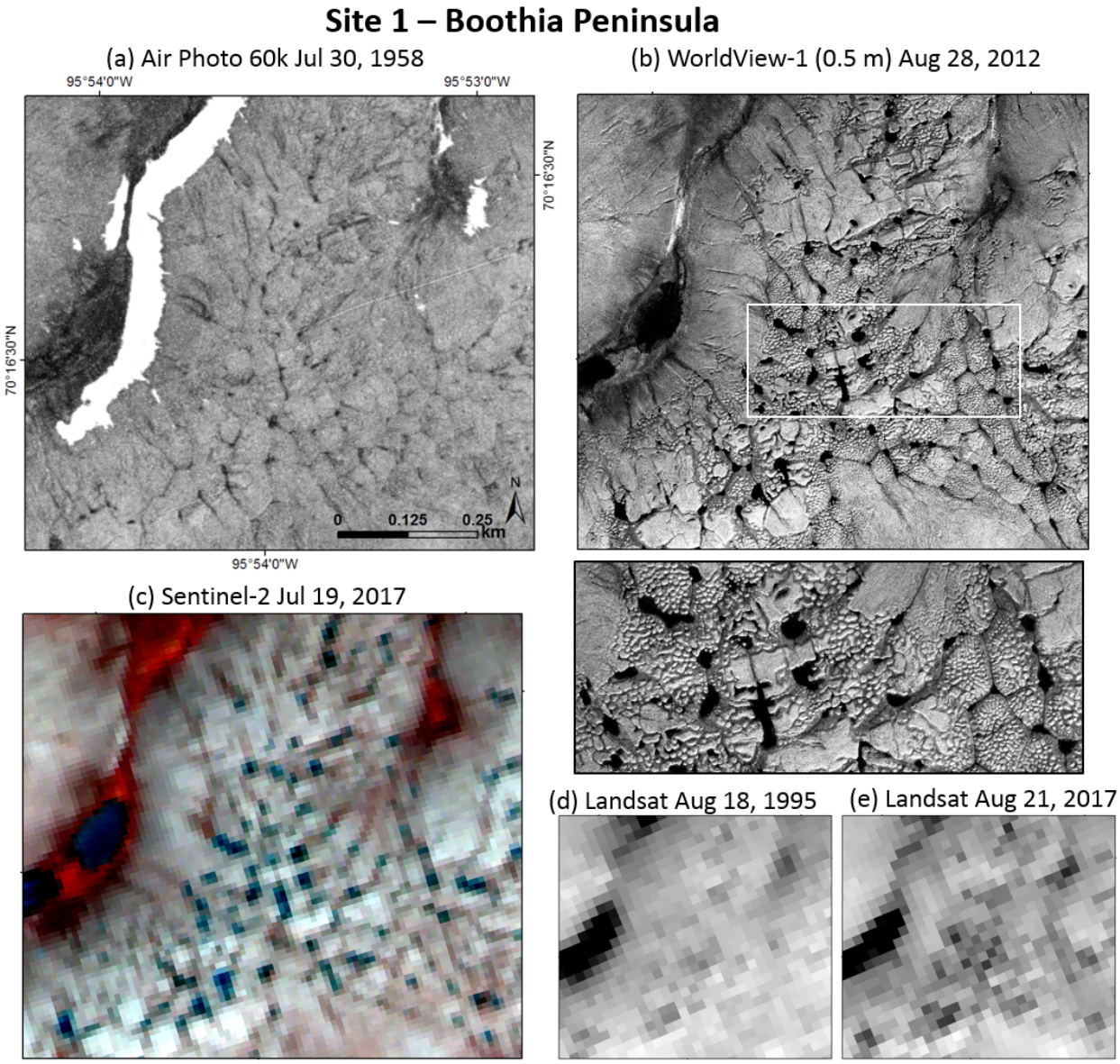

Site 3 – Somerset Island

(a) Air Photo 25k Jul 14, 1973

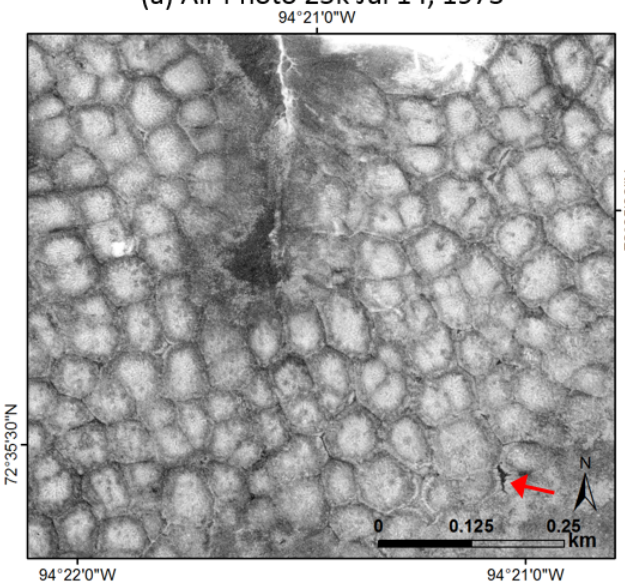

(b) WorldView-2 (0.5 m) Aug 19, 2012

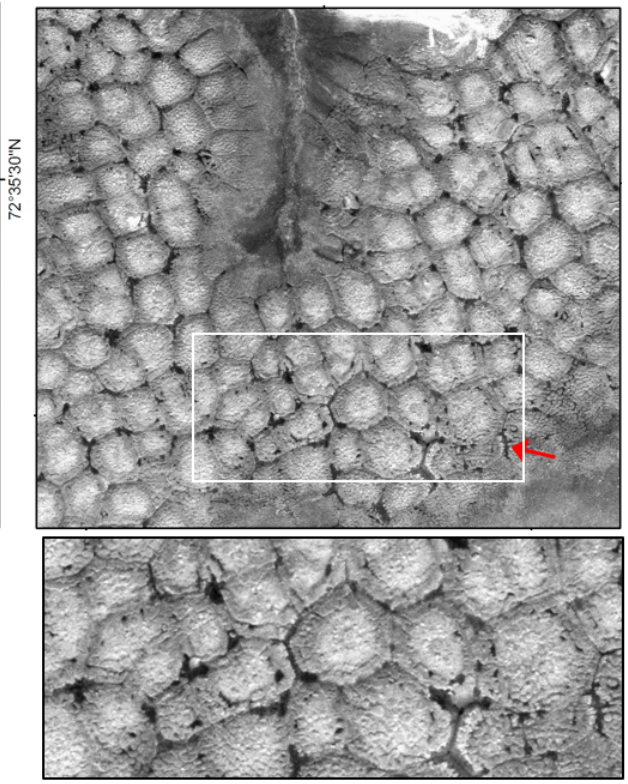

(c) Sentinel-2 Aug 12, 2017

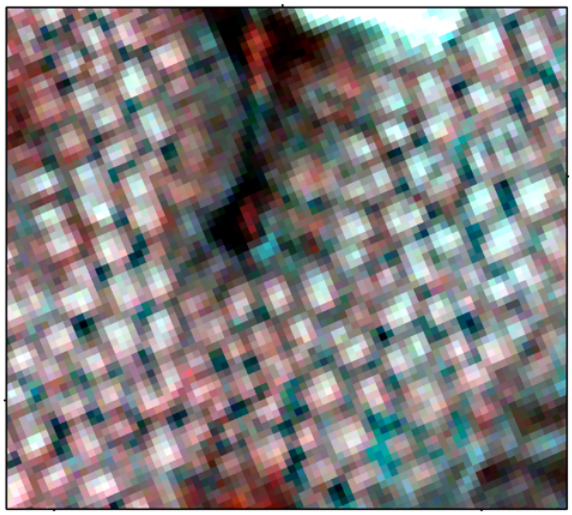

(d) Landsat Aug 14, 1986

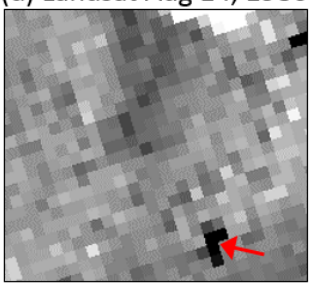

(e) Landsat Aug 2, 2016

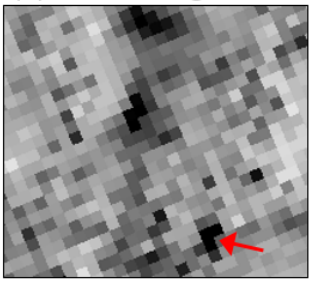

Site 4 – NE Victoria Island

(a) Air Photo 60k Aug 11, 1958

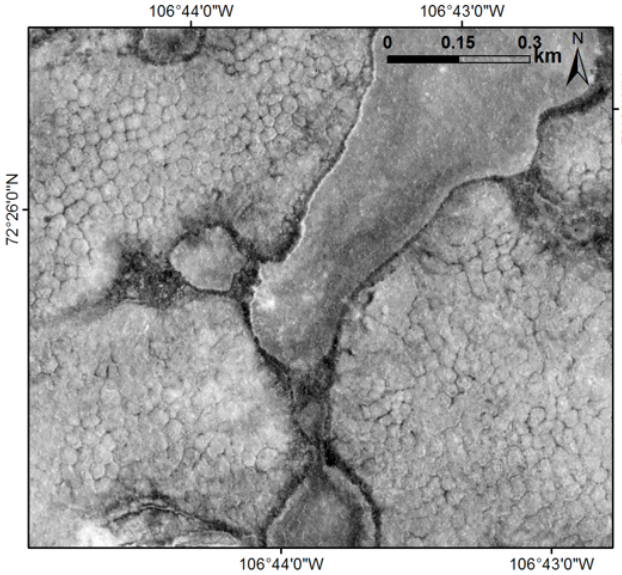

(b) WorldView-1 (0.5 m) Jul 16, 2015

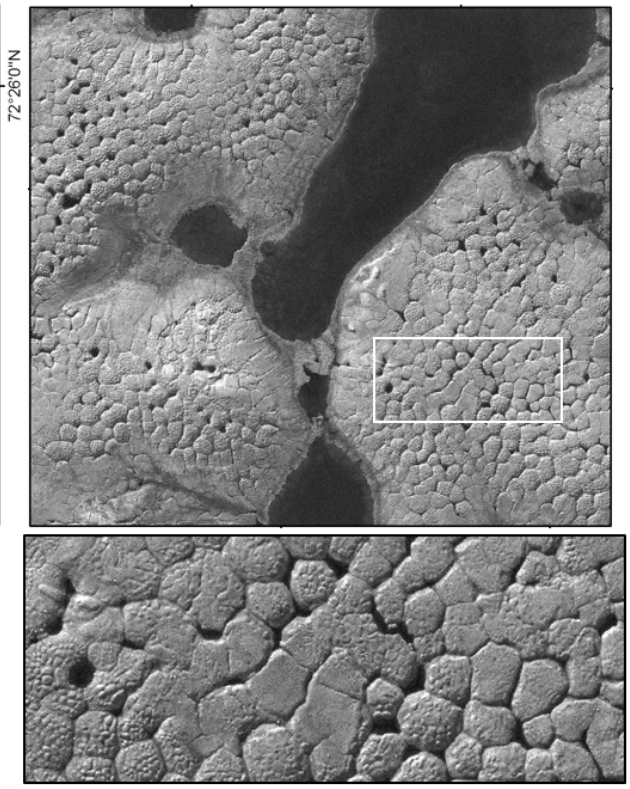

(c) Sentinel-2 Aug 29, 2016

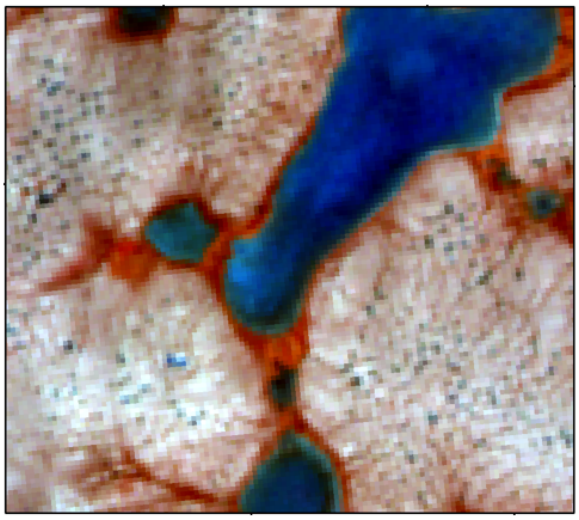

(d) Landsat Aug 8, 1992

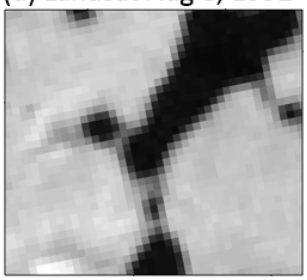

(e) Landsat Aug 9, 2013

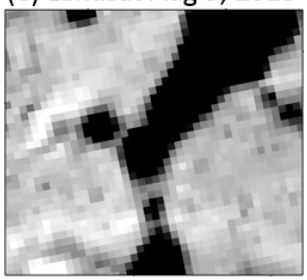

Site 5 – NW Victoria Island

(a) Air Photo 60k Aug 28, 1959

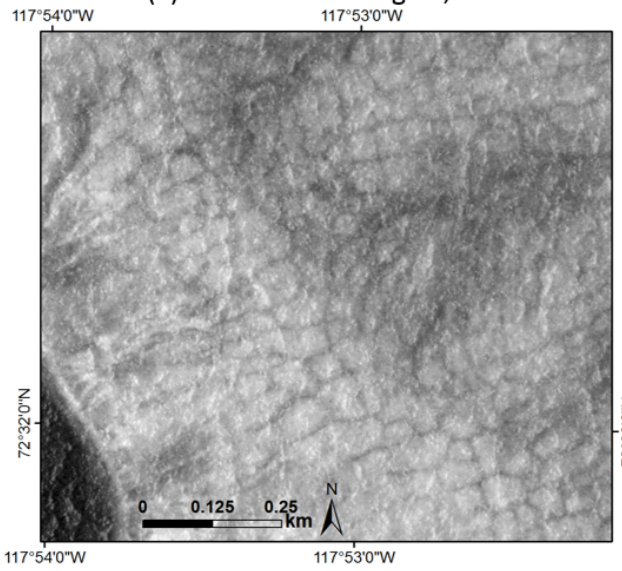

(b) Quickbird-2 (0.6 m) Aug 2, 2012

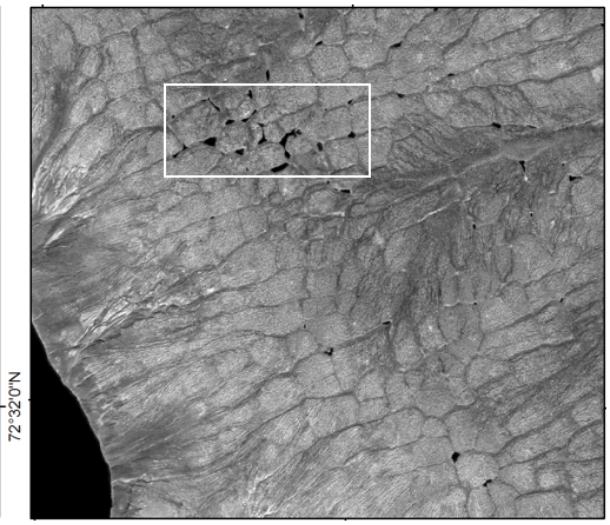

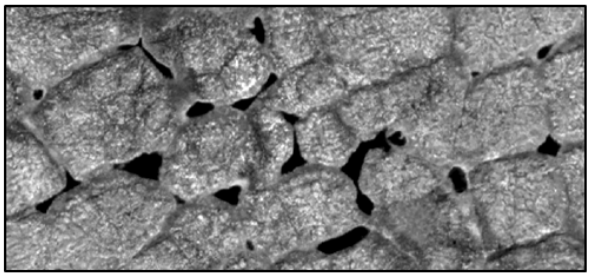

(c) Sentinel-2 Jul 19, 2017

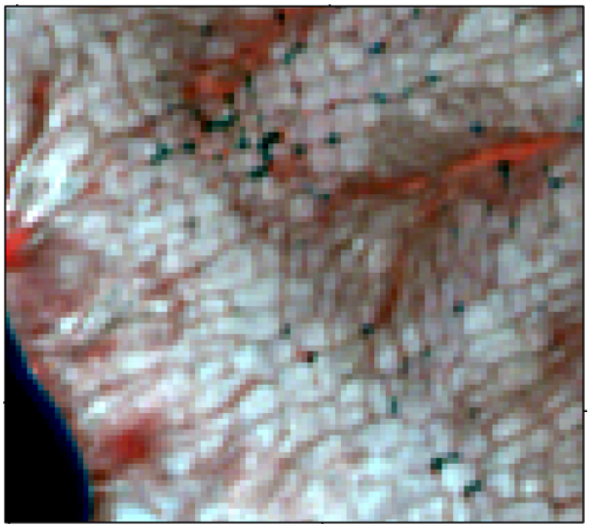

(d) Landsat Jul 24, 1992

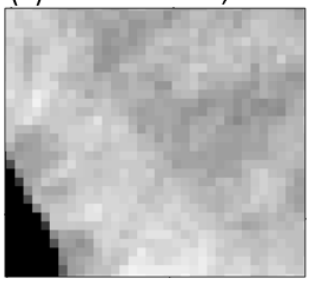

(e) Landsat Aug 3, 2013

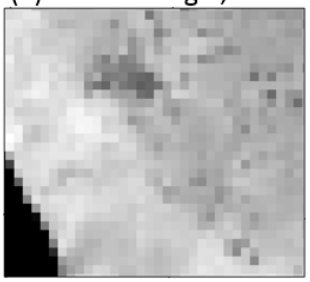

Site 6 – W Victoria Island

(a) Air Photo 100k Aug 10, 1961

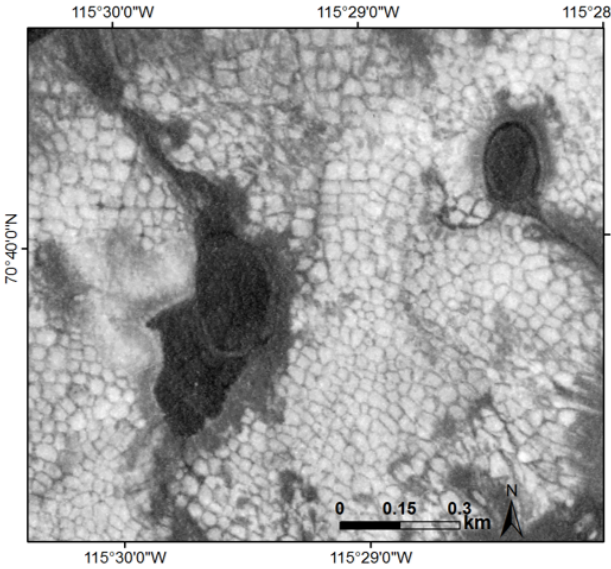

(b) WorldView-2 (0.5 m) Jul 19, 2014

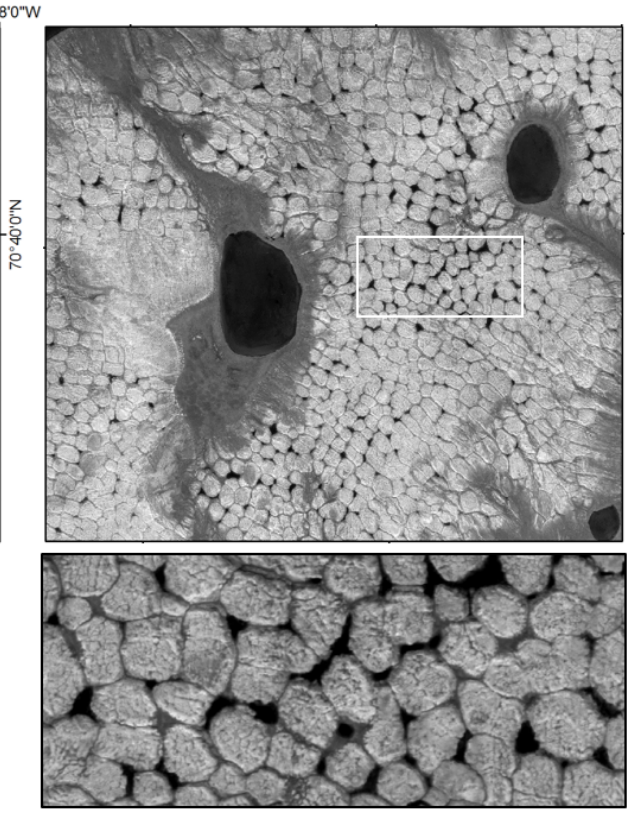

(c) Sentinel-2 Jul 20, 2017

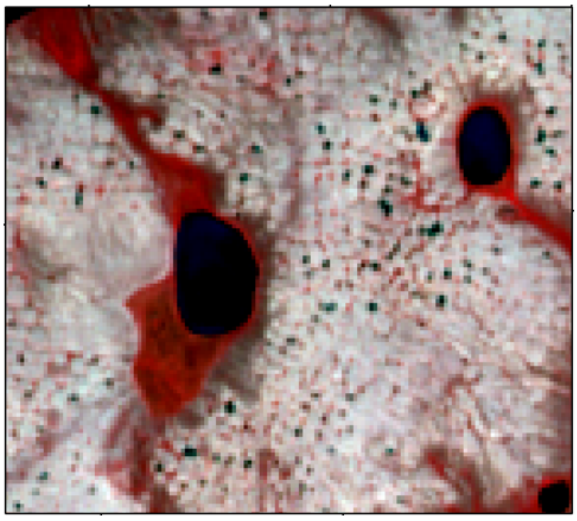

(d) Landsat Aug 21, 1989

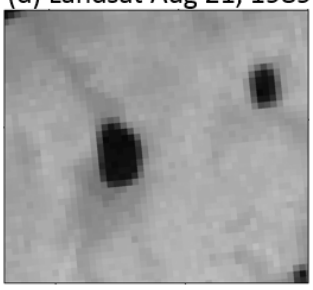

(e) Landsat Jul 28, 2016

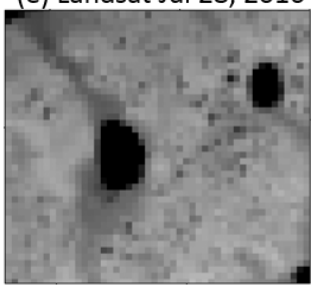

Site 7 – N Central Victoria Island

(a) Air Photo 60k Jul 15, 1958

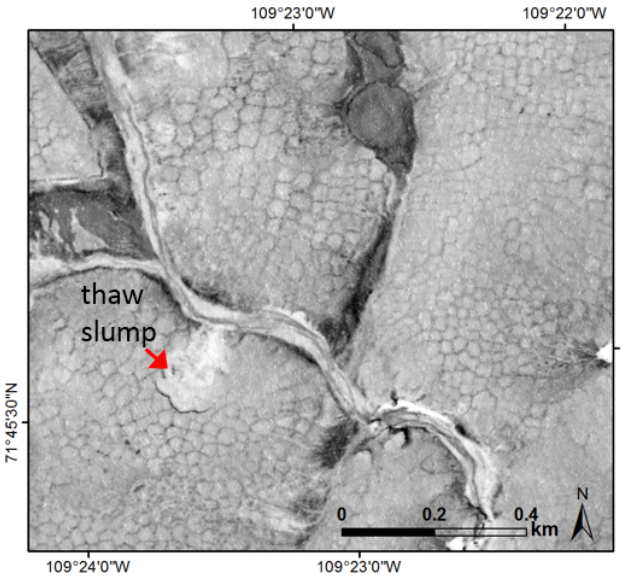

(b) Quickbird-2 (0.6 m) Aug 13, 2013

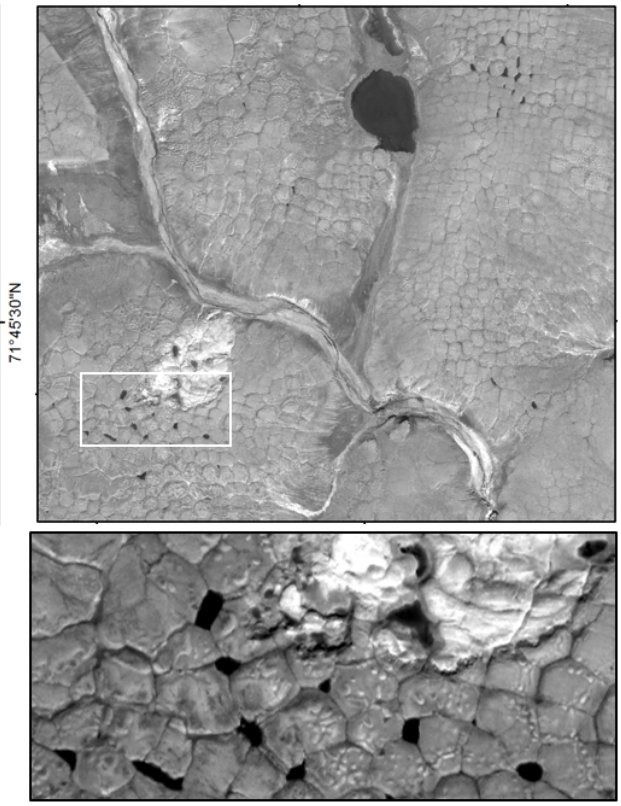

(c) Sentinel-2 Jul 14, 2018

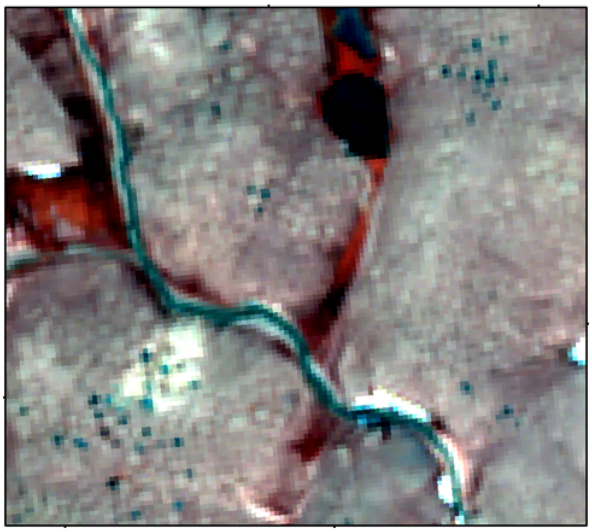

(d) Landsat Aug 21, 1989 (e) Landsat Aug 31, 2016

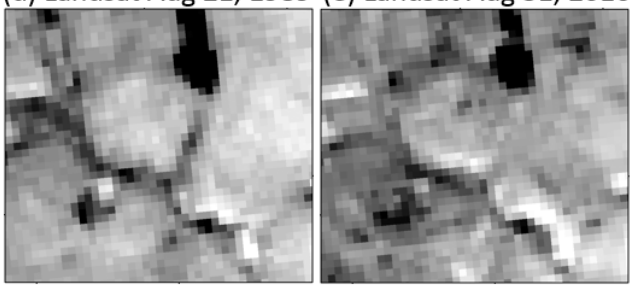

Site 8 – Tuktut Nogait NP

(a) Air Photo 60k Jul 23, 1974

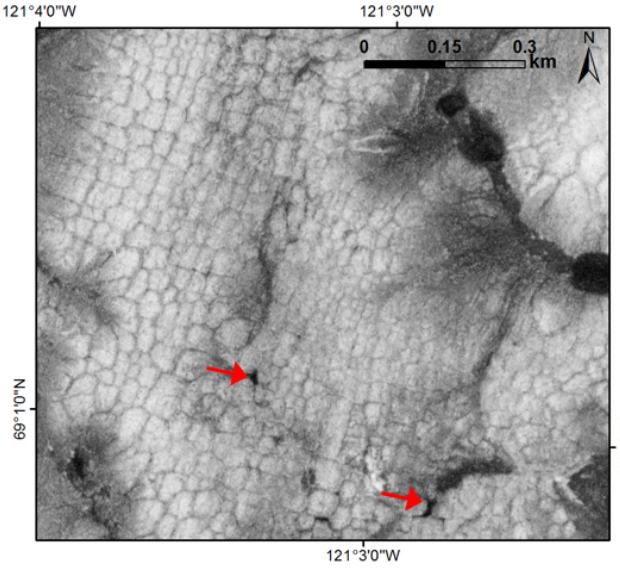

(b) GeoEye-1 (0.5 m) Aug 12, 2014

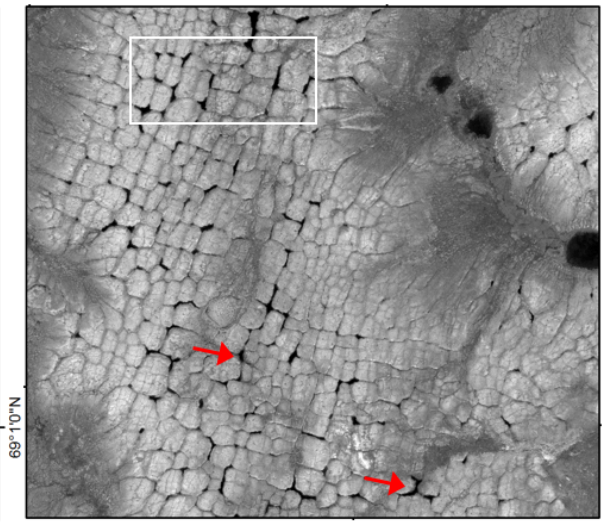

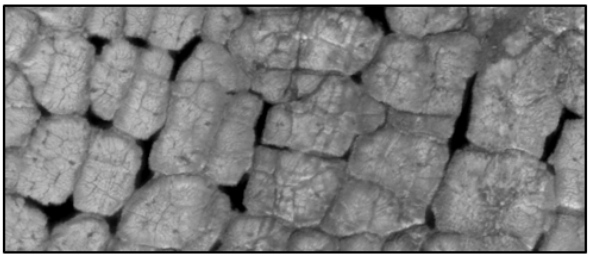

(c) Sentinel-2 Jul 12, 2017

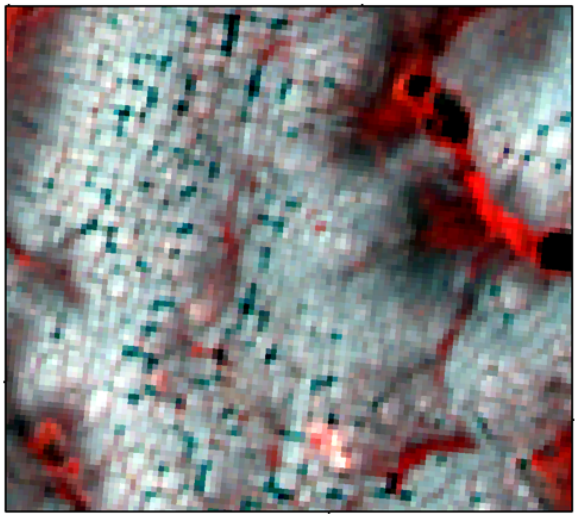

(d) Landsat Jul 29, 1988

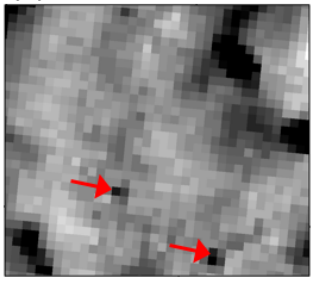

(e) Landsat Jul 18, 2013

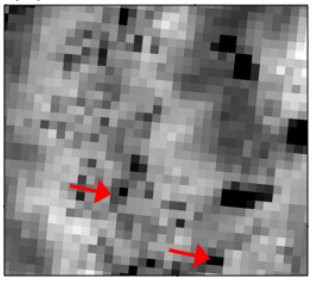

Site 9 – Yukon Coastlands

(a) Air Photo 25k Aug 28, 1970

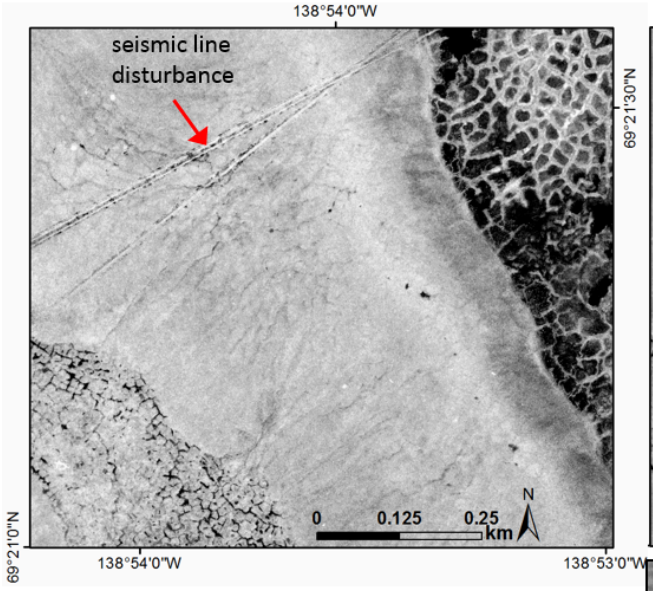

(b) WorldView-2 (0.5 m) Jul 23, 2018

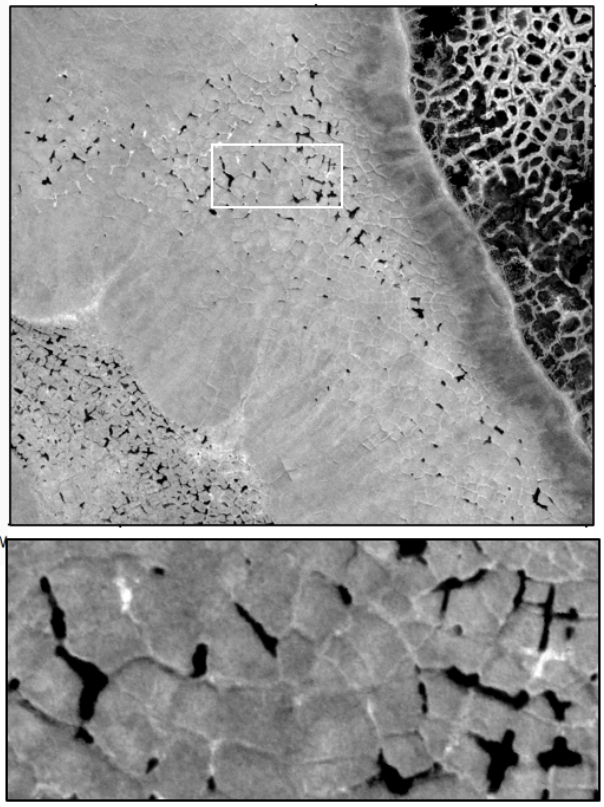

(c) Sentinel-2 Jul 28, 2017

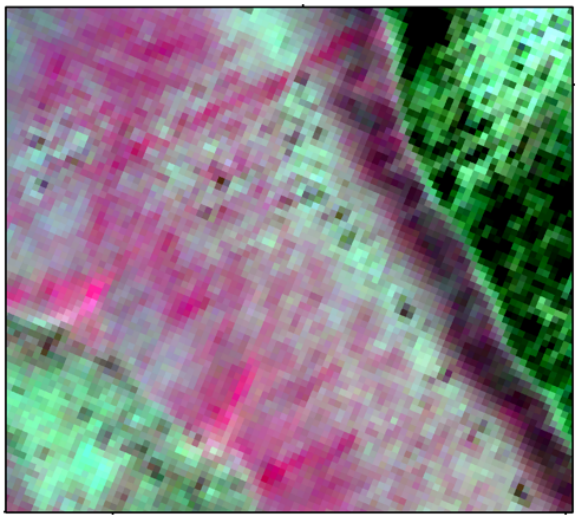

(d) Landsat Jul 12, 1986

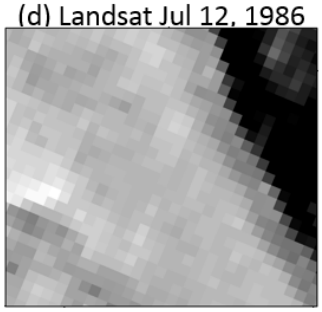

(e) Landsat Aug 6, 2016